ACS APPLIED MATERIALS & INTERFACES

Research Article

www.acsami.org

Fabrication of Macroporous Polymeric Membranes through Binary Convective Deposition

Alexander L. Weldon,[†] Pisist Kumnorkaew,[†] Bu Wang,[‡] Xuanhong Cheng,[‡] and James F. Gilchrist*[,†]

[†]Department of Chemical Engineering, Center for Advanced Materials, Engineered Particles Institute

[‡]Department of Materials Science and Engineering, Bioengineering Program, Lehigh University, 111 Research Drive, Bethlehem, Pennsylvania 18015, United States

Supporting Information

ABSTRACT: Binary convective deposition of silica/polystyrene under a number of different operating conditions is used to form nanoporous polymeric membranes with uniform and repeatable pore size throughout and across the membrane. One micrometer silica microspheres and 100 nm PS nanoparticles are codeposited from suspension under conditions where respective constituent fluxes are matched. Membrane thickness is controlled through single and consecutive monolayer and multilayer depositions. Consecutive monolayer depositions result in thin films with highest order and packing. Polymeric membranes were successfully fabricated from a continuous thin film by etching the SiO_2 microspheres with HF or KOH. Etching proceeds radially inward from the polymer−oxide interface suggesting that etchant/thin film interfacial energies help create the initial etching profile and drastically increase the overall etching rate. These membranes, of tunable pore size and functionality, will be ideal for targeted bioseparations specifically in the partition of pathogen particles out of blood suspensions.

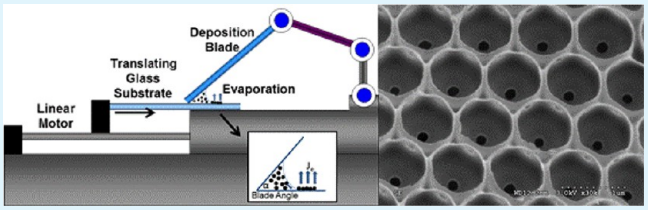

KEYWORDS: *polymer membranes, binary convective deposition, multilayer, silica, etching, polystyrene, melting, separations*

INTRODUCTION

Applications in biomedicine form one of the most important synthetic membrane market segments.[1,2] Nano- and microporous media with pore sizes comparable to bioparticles and biomolecules, i.e. mesopores (2−50 nm) and slightly larger, have found a wide range of utilities in biomedicine including biosensing,[3,4] targeted drug delivery,[5,6] immunoisolation,[7,8] dialysis,[9] tissue engineering,[10,11] bioseparation,[12,13] and bioanalytical[14] devices.

As size exclusion media, it is desirable to have membranes with pore sizes matching target sizes, from molecular to cellular scale, and high porosity. Conventional porous polymeric materials created by foaming, high internal phase emulsion (HIPE) polymerization, and phase separation[15] generally exhibit broad pore size distributions, random pore geometry, and are relatively thick.[16,17] As a result, these materials generally possess poor size cutoff properties and low transport rates. Alternate synthesis methods, such as track etching by nuclear fission fragments, have been developed to improve pore size distributions, pore structure, and pore geometry of polymeric membranes. These, however, face limitations of low porosity and random pore distribution. Other approaches to improve the physical properties of the mesopores include lithography and focused ion beam etching,[17−19] but these usually required sophisticated clean room facilities and sometimes have very low throughput. Membranes fabricated thorough block copolymer self-assembly followed by selectively etching the sacrificial blocks exhibit excellent biofiltration selectivity.[20] However, the pore size is limited by the self-assembled domain size, which ties to the macromolecular radius of gyration and is usually less than a few tens of nanometers.[21,22] Furthermore, composition of the block copolymer membranes is limited to those capable of forming segregation structures. Inorganic membranes synthesized electrochemically (e.g., anodic aluminum oxide),[23−25] by nanoparticle templating (e.g., porous silica),[26] or by self-assembly[27,28] have desirable physical structures and are scalable, but stiffness and lack of ductility make them hard to handle. In this study, binary particle suspensions were deposited through convective deposition in order to fabricate membranes that are highly selective with uniform[29] and well-defined pore size,[30] mechanical integrity,[31] and high potential for functionalization[32] and therefore are resistant to fouling.[33] Most membrane fabrication techniques are limited by one or multiple of these factors and/or scalability whereas convective deposition is enormously versatile in each regard[34]

Recently, a generic templating method has been proposed to fabricate porous membranes of versatile chemistry and with a broad range of pore sizes. The membranes are obtained through the selective removal of the porogen in a two-phase thin film.[35−37] The key step in this approach is to deposit particles controllably, which has been achieved with many methods including spin coating,[38] epitaxy,[39,40] optical tweez-

Received: May 5, 2012
Accepted: August 27, 2012
Published: August 27, 2012

   dx.doi.org/10.1021/am300785y | ACS Appl. Mater. Interfaces 2012, 4, 4532−4540

ers,[41] electrophoretic assembly,[42] and convective deposition.[43−45] Of these approaches, convective deposition yields regular particle layers quickly, controllably, and repeatedly. Convective deposition has been used previously for the formation of solid and porous thin films. Dip coating is a widely used and accepted technique for thin film fabrication. Boudreau et al. have used convective deposition through dip coating to assemble and grow zeolite layers on glass.[46] Bohaty et al. fabricated membranes through dip coating of glass substrates with SiO_2 particle suspension.[47] Extending beyond the idea of dip coating, a notably slow process, as a means of convective deposition, Yuan et al. fabricated mesoporous SiO_2 thin films through rapid convective deposition with a linear motor-driven evaporating meniscus.[48] However, these thin films were very thin and thus required fabrication atop a support. Advantages to the fabrication of membranes through convective deposition include the low cost of materials and equipment and the highly repeatable and versatile fabrication process as well as high porosity. By selecting appropriate matrix chemistry or surface modification post fabrication, the membrane can be rendered resistant to fouling and resilient under backflushing or crossflow. Convective deposition gives large flexibility in terms of materials and the potential to functionalize membranes and enhance bioseparations. The aforementioned research by Boudreau et al. as well as Bohaty et al. show the successful functionalization of assembled zeolite and SiO_2 films through silane treatments respectively.[46,47] Also, Lee et al. perform enantiomeric drug separations with antibody-functionalized alumina membranes and Létant et al. use biotin-functionalized silicon membranes to capture particles modeling viruses and bacteria.[13,49]

In this study, convective deposition was used to create crystalline thin films containing two types of particles, nanoparticles that remain as the polymeric membrane and larger microspheres that are sacrificed to form the cavities and pores. A thin film consisting of ordered SiO_2 microspheres and polystyrene (PS) nanoparticles was codeposited with highly uniform local microstructure, long-range morphology, and film thickness. After melting the PS particles and etching away SiO_2, a continuous PS porous phase was obtained. This convective deposition process involves the translation of a meniscus of suspension across a glass substrate under a glass blade. Prior work on convective assembly studies the self-organization of particles and how factors like blade angle and hydrophobicity, as well as deposition speed and glass treatment, affect the resultant thin film.[50] This method was used to fabricate composite thin films by consecutive depositions of SiO_2 microspheres followed by polystyrene (PS) nanoparticle depositions in order to dramatically improve the light extraction efficiency of LEDs.[50] Lenhoff and Velev describe the gravitational sedimentation of template colloidal crystals. Infiltration of a second constituent, and subsequent removal of the template, leaves behind a porous structure.[51] Alternatively, as used in this study, both the oxide and polymer phases can be codeposited in one deposition; these binary depositions yield crystalline monolayers with long-range order only when microsphere and nanoparticle component fluxes are matched.[52] The key difference between this study and previous studies is that this codeposition decreases the complexity of the membrane fabrication process, increases the ability to control membrane fill fraction, scales up easily, and is consistent over longer ranges than consecutive unary depositions.

The convective deposition of binary suspensions is an ideal method for the repeatable fabrication of membranes with uniform[29] and prescribed pore sizes,[30] ordered microstructure, targeted morphology, and customizable thickness. Through tuning the sizes of the larger and smaller constituents it is simple to optimize membrane pore size for particular applications. Advantages to the fabrication of membranes through convective deposition include the low cost of materials and equipment and the highly repeatable and versatile fabrication process. These membranes are highly porous while remaining mechanically strong.[31] They also hold a high potential for functionalization[32]and therefore are resistant to fouling[33] and are resilient under crossflow or backflushing. Most membrane fabrication techniques are limited by one or multiple of these factors and/or scalability, whereas convective deposition is enormously versatile in each regard.[34]

MATERIALS AND METHODS

Suspensions Preparation. The silica/polystyrene (SiO_2/PS) binary suspension used in these membrane fabrication experiments was produced through the combination of unary SiO2 and PS suspensions. The SiO_2 suspension consisted of SiO_2 microspheres (Fuso Chemical Co, Japan) dispersed in deionized (DI) H_2O. These fused microspheres are of density 2.2 g/cm^3, have average diameter $2a_{micro}$ = 1.01 ± 0.02 μm, and ζ-potential of −48 mV ± 1 mV (Pen Kem Model 501 Lazer Zee Meter). The PS suspension consisted of $2a_{nano}$ = 100 nm PS nanoparticles (Emulsion Polymer Institute, Lehigh University) in DI H_2O having ζ-potential of −59 mV ± 1 mV. Concentrated individual stock suspensions of SiO2 and PS were prepared (30% and 25%, by volume, respectively), dispersed using a sonic dismembrator (model 550, Fisher Scientific, Pittsburgh, PA), then used along with additional DI H_2O to make the 20% volume fraction SiO_2 and 8% volume fraction PS colloidal suspension used in these experiments.

Substrate Preparation. Glass microslides (Fisher Sci. Plain Glass Microscope Slides Premium, 76 × 25 × 1 mm^3) were used as deposition blades and substrates. All substrates were cleaned by immersion in piranha solution with a 5:1 ratio of sulfuric acid/hydrogen peroxide overnight. After cleaning, the microslides were rinsed with and stored in DI H_2O. The bottom edges of the deposition blades are coated with parafilm (Fisher Sci.) to make that edge hydrophobic. Contact angles of 10 μL drops of 20% 1 μm SiO_2/DI H_2O suspension are measured on glass slides and parafilm at 10 and 105°, respectively. Contact angle experiments were measured through imaging of sessile droplets on glass.

Convective Deposition. The experimental setup is described previously.[50] All experiments were performed at 50% ± 5% relative humidity and 24 °C. The blade angle was fixed at 45° and positioned 10 μm above the substrate for all experiments and 10 μL suspension volumes were injected between the blade and substrate for each experiment.

Polystyrene Melting. Polystyrene in convectively deposited thin films was melted using a Fisher Scientific hot place set at 250 °C for 20 min.

Etching. SiO_2 was etched from SiO2/PS thin films using Hydrofluoric Acid (HF, 49%, Sigma Aldrich) or Potassium Hydroxide (KOH, extra pure flakes, 85%, Acros Organics). HF etching was carried out using 12% HF/DI H_2O bath for 5 min at room temperature. KOH etching was carried out using 30% and 40% KOH/DI H_2O at room temperature, 80 °C, and 90 °C on a hot plate for up to 72 h. HF-etched membranes were rinsed in ethanol while KOH-etched membranes were rinsed with DI H_2O.

Microstructure Analysis. Fabricated membranes were analyzed primarily through scanning electron microscopy on a Hitachi 4200 field emission SEM with some quick imagery performed on available optical and confocal microscopes. Relevant data presented here was gathered on the SEM at nominal horizontal orientation while tilted to show membrane height and intermediary structure. Pore sizes were

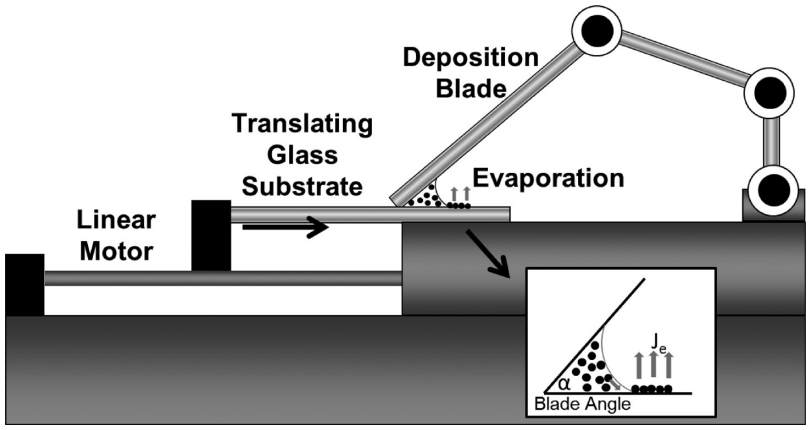

Figure 1. Schematic drawing of convective deposition setup (not to scale). Suspension is injected between a glass substrate and hydrophobic deposition blade. The substrate is then linearly translated, as indicated by the horizontal arrow, and evaporation-driven flux leaves behind a particle thin film.

measured from SEM imagery using ImageJ. Prior to electron microscopy samples were coated with Iridium using an EMS, Electron Microscopy Sciences, 575X Turbo Sputter Coater.

RESULTS AND DISCUSSION

Aspects of convective deposition and etching were explored in order to fabricate robust membranes with high porosity and uniformly sized and spaced pores. In overview, colloidal crystal structures were first assembled on a glass substrate by convective deposition of a binary suspension of 1 μm silica (SiO_2) microspheres with 100 nm polystyrene (PS) nanoparticles. Previous research on the formation of microsphere monolayers and multilayer colloidal crystal self-assembly[50,52,53] gives a basis for these experiments. Melting the polymer nanoparticles forms the working membrane, providing a uniform, continuous scaffold around the SiO_2 microspheres. Next the SiO_2 is etched from the colloidal crystal with KOH or HF. While in principle only a single crystalline layer would be needed to form a uniform membrane with controlled pore size, in practice such a layer is too thin and fragile to be easily handled or effectively used under real filtration conditions with a significant transmembrane pressure drop. The viability of this work is shown through proof of concept experiments as well as closer examination into multilayer and layer by layer depositions to fabricate membranes of controllable thickness without losing the repeatable crystal structure and consequent uniformly sized and shaped pore/cavity sizes.

Colloidal Crystal Formation. Membrane fabrication strategies focus around permutations of successive monolayer or multilayer depositions of binary suspensions. As shown previously, subsequent microsphere particle depositions align to fill the interstices of their base layer and grow the crystal.[50] Binary deposition gives the ability to deposit a two-phase layer, which is critical in the fabrication of these microporous membranes. Also, the addition of a smaller constituent alongside the SiO_2 microspheres greatly enhances packing and thin film uniformity making for an enormously repeatable fabrication process.[52,53] Membranes were synthesized with thicknesses ranging from a single (monolayer) to six layers of SiO_2. The relationship between the deposited crystal thickness and deposition rates is coupled through a simple mass flux balance, eq 1, first posed by Dimitrov and Nagayama[43] as

$$v_{mono} = \frac{J_e \beta}{2a(f)} \frac{\varphi}{(1-\varphi)} \quad (1)$$

Here, v_{mono} describes the substrate velocity for monolayer deposition that depends on J_e, solvent flux; $2a$, microsphere diameter; φ and f, which are the suspension volume fraction and volume fraction within the deposited thin film respectively; and β, a parameter describing particle-surface interactions; $\beta \approx 1$ when particle−surface interactions are strongly repulsive as is the case in this study using highly repulsive constituents and substrates. At faster deposition speeds than v_{mono}, the substrate translates faster than the crystal formation rate and results in submonolayer morphology. Conversely, at deposition speeds slower than v_{mono}, the rate of particles flowing to the crystal formation front exceeds the deposition velocity and a resultant multilayer is formed. Previous work[50] shows that other factors such as the shape of the meniscus dictated by the blade angle α (shown in Figure 1) also influence the deposition rate.

For these experiments, the monolayer deposition speed for the binary SiO_2/PS suspension was determined to be v_{mono} = 40.8 μm/s through confocal and scanning electron microscopy. The deposition speed can be altered to deposit crystalline multilayers of targeted thickness. For instance, depositing at one-half the monolayer velocity, 1/2 v_{mono}, will deposit two layers, 1/3 v_{mono} will deposit three, etc. Surprisingly, this holds although the primary mechanism for assembly during deposition changes between monolayer and multilayer deposition. Assembly in monolayer deposition is driven by capillary interactions of particles confined within a film of thickness on the order of the particle size. In multilayer deposition, the relatively thick film is filtered through the growing crystal and assembly primarily occurs due to pressure-driven 'steering'.[54] However, the most dense and ordered crystalline membranes are produced with depositions speeds close to v_{mono}. Multilayer depositions, as their name suggests, result from multiple particles flowing at once to the crystal formation front. The initial layers of particles formed on the substrate show high packing and long-range crystallinity; however, additional particles flowing in (arranging atop that first layer) have trouble arranging with maximal order. Two strategies, consecutive and multilayer depositions, were explored in combination and independently to increase membrane thickness. Multilayer depositions can be performed at any fraction of v_{mono} in order to control layer thickness.

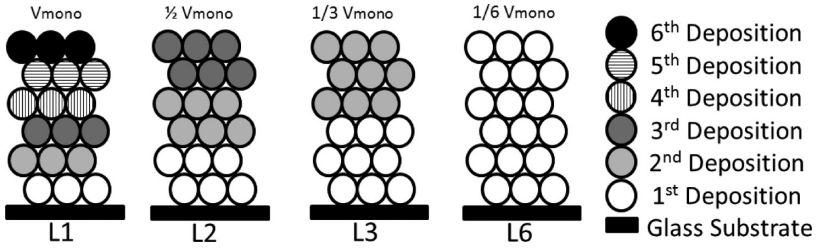

Figure 2. Sketch showing the deposition strategies developed through an understanding of the direct relationship between deposition speed and crystal formation rate. V_{mono} is the monolayer deposition speed determined to be 40.8 μm/s From left to right, L1 comprises six consecutive monolayer depositions at v_{mono}, L2 comprises three consecutive bilayers deposited at 1/2 v_{mono}, L3 comprises two consecutive trilayers deposited at 1/3 v_{mono}, and L6 comprises a single six-layer deposition deposited at 1/6 v_{mono}. Note L1, L2, L3, and L6 have identical thickness but may vary in structural periodicity and crystallinity.

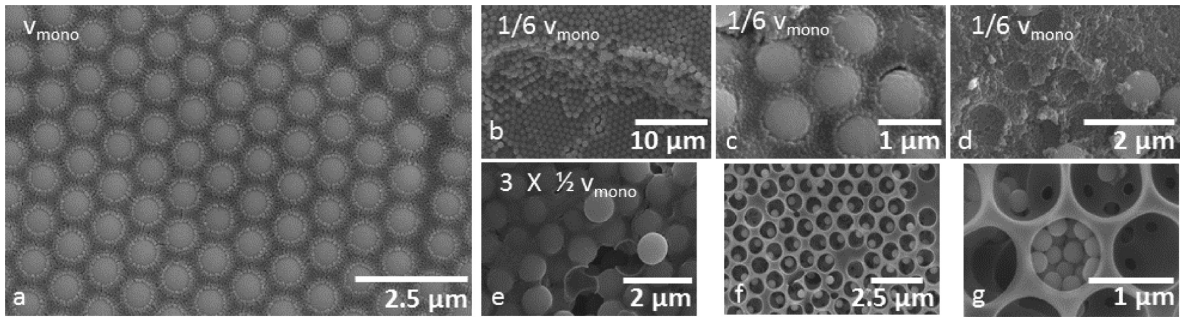

Figure 3. (a) Well-ordered single layer of SiO_2/PS, (b–d) unmelted SiO_2/PS layers deposited at 1/6 v_{mono}, L6, (e–g) melted SiO_2/PS layers deposited at 1/2v_{mono}, L2, as well as (c–g) progressive partially etched samples. (b) Image showing progressive multilayer morphology with underlying highly ordered layers in a razor-scratched sample. c–e have been etched in 30% KOH for <12 h at 80 °C without melting PS. c and d show partially etched samples with unmelted PS. Notice that in c, the SiO_2 spheres are beginning to etch away, and in d and e, the partially etched spheres have etched to the degree that they can lift off from the layer. e shows a sample partially etched similarly to c and d with similar microsphere liftoff but from a melted PS scaffold. f and g represent incomplete etching under 17 h 40% KOH etching at 90 °C with a melted PS scaffold. f shows the recedence of the SiO_2 microspheres under etching sitting in each cavity with the cavities' associated pores in view as well. g shows that the etched SiO_2 microspheres are in fact free-floating having washed out of a number of neighboring cavities and redeposited into a single void.

Monolayer depositions can increase membrane thickness very controllably one layer at a time. As a natural extension, multiple particle multilayers can be deposited to thicken membranes in fewer steps. Samples fabricated at slightly faster deposition speeds than v_{mono} show somewhat less uniform crystallinity and more defects at the local level though they are still composed primarily of crystalline regions. With increasing speed, these submonolayer depositions show an increasing prevalence for void patches as well as particle patches, bands, and strings.

Particles were deposited at one, one-half, one-third, and one-sixth the monolayer deposition speed. In each case, the aim was to make a membrane six layers thick; thus depending on the deposition speed, six depositions for v_{mono}, three for 1/2 v_{mono}, two for 1/3 v_{mono}, and one for 1/6 v_{mono} were performed (Figure 2). This thickness was chosen to show the tunability of convective deposition as a membrane fabrication technique process and because these membranes were thick enough so as to be mechanically strong and easy to handle. One point to be considered is that, given the finite suspension volume in each experiment, controlling the flux so as to increase the number of vertical layers leads to a corresponding decrease in deposition length and resultant shorter membrane. Here, semibatch processing using a finite volume of suspension was employed. Ten microliters of SiO_2 suspension 20% volume fraction yield roughly 4 × 2.5 cm^2 depositions at v_{mono}, whereas those run at 1/6 v_{mono} were roughly 0.7 × 2.5 cm^2 in length.

Template Etching. To convert microsphere crystal assemblies into membranes, we treated SiO_2/PS thin films with Potassium Hydroxide (KOH) or Hydrofluoric Acid (HF). Using KOH as an etchant, usable well-ordered membranes are fabricated under all deposition conditions. Even in depositions having defects or disorder, the membrane will still be composed of cavities and pores of equal size and thus will have identical separations capability with regard to size selectivity, as shown in Figure 3f. Figure 3a shows a binary monolayer deposition of SiO_2/PS with a second PS monolayer deposition. Note the crystalline structure of the particles. Occasional line and point defects do form but, by and large, a hexagonal close-packed microstructure is maintained. Here an additional 8% volume fraction PS/DI H_2O deposition was performed atop the SiO_2/PS thin film demonstrating the ability to form a fully connected continuous membrane in the event PS was not uniformly distributed through the SiO_2 crystal or was not present in sufficient quantities to fully cover the SiO_2 microspheres. The nanoparticles flow uniformly into the interstices and show that additional depositions do not disrupt the base layer. This additional deposition ended up being unnecessary as sufficient PS is deposited with both multilayer and consecutive binary depositions to form mechanically robust membranes. This unary PS deposition step is omitted from all subsequent membrane fabrication experiments.

Increasing the thickness of the SiO_2/PS thin films while maintaining uniform pore size and membrane morphology is next explored. Figure 3b–d shows membranes fabricated through a single binary deposition at 1/6 v_{mono}. Note the differences in crystallinity between the bottom and top layers of

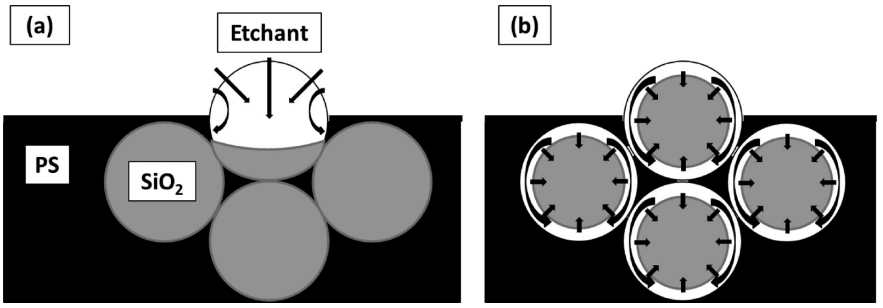

Figure 4. Sketch showing two alternative mechanisms by which SiO_2/PS membranes might be etched. (a) Top-down etching process whereby the underlying SiO_2 microspheres will not be etched until their top neighbors have receded sufficiently. (b) Method where the etchant works its way around the microspheres, flows through pores, and etches multiple layers simultaneously. The microspheres recede inward uniformly from all sides and are freed to liftoff and potentially leave their cavities. Imagery in Figure 3 supports method b as the mechanism of etching.

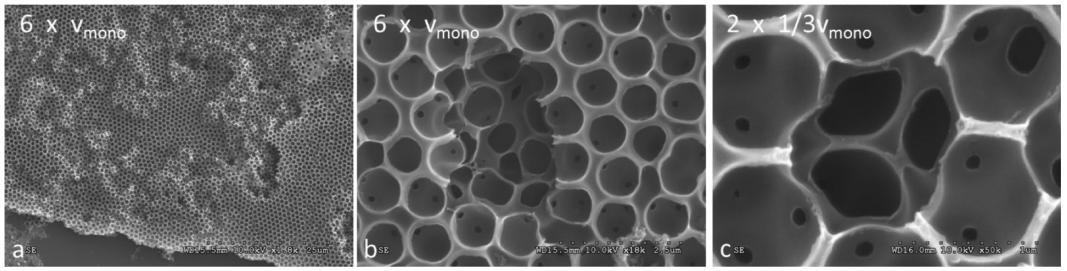

Figure 5. SEM Images showing the robustness of our membrane fabrication process. (a, b) Synthesized through six consecutive depositions at v_{mono}, L1; (c) synthesized with two depositions at 1/3 v_{mono}, L3. All three images show that in the sparse defect regions supporting underlayers obviate any potential weaknesses of the membrane. Note that samples a and b were scratched with a razor in order to evaluate membrane interior and the especially large amounts of nonuniformity in the top layers is a product of that scratching process.

the thin film. The bottom layer is very well-ordered and crystalline but moving vertically through the deposition there is an increasing degree of nonuniformity. The top layer shows smaller crystalline regions without the long-range order of their lower neighbors. The result is a semiunconnected network of SiO_2 microspheres that renders the process ineffective for fabricating a working membrane. Figure 3c–e has been etched for <12 h with 30% KOH/DI H_2O at 80 °C. In Figure 3c, where the PS is unmelted in an attempt to enhance the etching of interior SiO_2 microspheres, only slight recession of the SiO_2 microsphere surface is found. As the process continues in Figure 3d, the microspheres etch to the degree that they become free-floating, exit, and leave behind resultant void regions in the PS membrane.

The microspheres maintain their spherical shape under etching indicating that etching proceeds uniformly from all sides rather than in a purely top-down format (Figure 3f, g). These samples have been etched for 17 h with 40% KOH/DI H_2O at 90 °C. In Figure 3f the SiO_2 particles have recessed significantly; Figure 3g shows the same behavior but highlights the fact that the particles are in fact freestanding in their cavities. Here multiple SiO_2 nanoparticles have recessed, detached, and lifted off only to redeposit in single void. Imaged f and g in Figure 3 highlight the size exclusion properties of these membranes and the robustness of the pores during the etching process. The particles are effectively filtered and not allowed to pass through. For an application of virus separation from blood cells, cellular constituents larger than these shrunken particles would be stopped, whereas the virus components, on the order of a hundred nanometers or smaller, could easily pass through. Figure 4 describes two potential mechanisms for etching. In the first, etching proceeds through a top-down process where SiO_2 microspheres in the top, exposed, layers etch initially. Only when the exposed microsphere is sufficiently etched away can the KOH flow to microsphere-microsphere contact point and begin to etch the next microsphere. However, that the SiO_2 microspheres, collected in that PS cavity, remain monosized the etching process as they shrink sufficiently to escape their original PS cavities indicates that a second mechanism governs the etching process. That the melted PS is essentially nonpermeable indicates that the etchant creeps along the sides of the microspheres and thus etching most likely proceeds simultaneously in all layers at once. A possible explanation of this is the fact that SiO_2/KOH surface energy is much lower than SiO_2/PS surface energy and thus KOH selectively wets along the microsphere/scaffold interfaces and flows from microsphere to microsphere under a faster time scale than the etching itself (Figure 4). Aided by the increase of surface energy, the entire surface area of the microspheres is simultaneously etched inward. Crude contact angle of 40% KOH/DI H_2O measured on glass are roughly <10°, whereas the observed wetting angle of PS on the microspheres as calculated from SEM imagery is roughly 40°. As a side note, the increase in SiO_2 microsphere etching is due to the longer etching time and higher temperature. It is not due to the increase in KOH concentration.[55]

Optimizing suspension characteristics should provide great control over membrane pore sizes. To validate this hypothesis, we synthesized membranes with 1 μm SiO_2/100 nm PS and 0.5 μm SiO_2/100 nm PS. For each membrane, two types of pores were evaluated: microsphere–microsphere intercavity pores and microsphere–substrate pores (see the Supporting Information, Figure S1). As expected, the larger particles yielded larger pores. One micrometer SiO_2/100 nm PS exhibit 141 ± 10 nm (one standard deviation) intercavity pores and 200 ± 8

nm pores at microsphere-substrate contact points. 0.5 μm/100 nm PS exhibit 103 ± 5 nm intercavity pores and 149 ± 8 nm pores at microsphere−substrate contact points. Obviously the smaller pores will govern membrane selectivity. The difference in pore sizes stem from the differently sized interstices between microspheres and their neighbors versus microspheres and the substrate—we hypothesize that a combination of nanoparticle packing and polystyrene wetting ability on SiO_2/glass within these angles governs the difference. In addition to particle size, constituent composition can be varied. Preliminary trials with polyethylene glycol (PEG) MW 575 and MW 258 were performed. Crystalline SiO_2/PEG layers can be deposited, with the PEG cured under UV, but a higher degree of heterogeneity in the deposition and initial trials to selectively remove the SiO_2 phase generated lower quality films. The success of PS trials does give validity to the potential of future research into alternative polymers.

Figure 5 highlights the robustness of this membrane fabrication technique. Here all membranes have been fully etched with 40% KOH for >24 h at 90 °C and subsequently rinsed with DI H_2O. These images show the strength of repeating layers of pores in a multilayer membrane. The large and deep defect regions, excellent for showing underlying layers and presented in images a and b in Figure 5 respectively, are not typical of mono- and multilayer depositions and instead are created, in the sample preparation process, to present uniform lower layers and cavities. Close inspection shows that the enormous stress of fracturing the membranes, in Figure 5a, has affected only the top two, fifth, and sixth membrane layers; the untouched visible underlying pore array in Figure 5a is the fourth layer. Figure 5b shows a deeper defect, also near the fracture zone, and shows that layer defects are compensated by their underlying neighbors such that neither the integrity of the membrane nor its separations capabilities will be impaired. Figure 5c specifically shows a point defect, in the original deposition, with the crystalline layer below obviating any potential filtration issues. This robustness and mechanical stability to the fabricated membranes will contribute to their longevity and long-term effective filtration. Specifically, in presence of a defect or membrane stress, the low propensity for that crack to propagate will both limit decreased membrane effectiveness and prevent catastrophic failure.

Figure 6 shows membranes fabricated under optimal conditions. Note the higher order of the topmost layers as compared with the slower multilayer depositions. These membranes, fabricated through multilayer and monolayer depositions, have identical pore and cavity sizes; however thin films fabricated through multiple consecutive monolayer depositions show the highest crystallinity and packing and thus would be expected to have the highest resolution selectivity in filtration applications. The membranes presented in Figure 6 are fabricated through six consecutive depositions at v_{mono}, 24+ hs of 40% KOH etching at 90 °C, and four DI H_2O water washes/soaks. These membranes are presented at progressively lower magnifications in order to highlight first the regular orientation of the pores and second the high crystallinity and low number of defects across the membrane. Note that the submonolayer patchiness in the top layer is a product of the consecutive depositions. In depositions on bare glass or other hydrophilic flat surfaces, a monolayer deposition deposits exactly that: a single layer of particles with very long-range order and high crystallinity.[50,52,53,56] To confirm the regularity of the membrane interior, Figure 6d shows a fractured

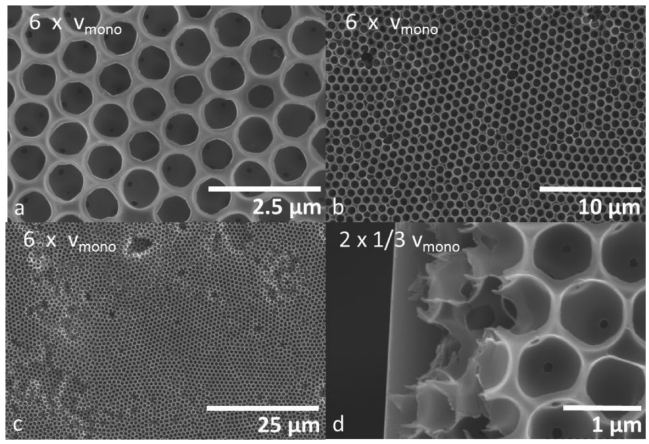

Figure 6. (a−c) Fully etched membranes at progressively lower magnifications fabricated with six consecutive depositions at v_{mono}, L1, etching with 40% KOH/DI H_2O for 24+ hours at 90 °C, and four water bath washes/soaks. In a, note the pores connecting the topmost sets of cavities to their neighbors underneath at points where SiO_2 microspheres previously touched. In b and c, note that even in defect regions, where the uppermost layer or two exhibits submonolayer characteristics as a product of the somewhat rough surface of underlying crystalline SiO_2, the underlying layers maintain the integrity of the membrane. (d) Interior of a membrane fabricated with two 1/3 v_{mono}, L3, depositions. This sample is placed atop a glass slide and the slide and membrane are snapped in half. The SEM stage is tilted in order to highlight the membrane interior. Note the visible cavities with their pores in the interior of the membrane. Also note that the infrastructure of the membrane is intact; this highlights the mechanical strength of the PS membranes.

membrane, fabricated through two consecutive depositions at 1/3 v_{mono}, viewed on a tilted SEM stage. It highlights the interior structure of the membrane including partial voids along the fracture plane. These images show the mechanical stability of the membranes in that the membranes fracture cleanly without fingers or cracks extending inward from the fracture line. Also note that this fracturing method of snapping the substrate and thin film disrupts the structure of the topmost membrane layers far less than the razor-scratching membrane presented earlier.

KOH etching successfully produced robust, uniform membranes; the only downside to KOH etching is the higher temperature and long time necessary to successfully remove SiO_2 microspheres. As such the next step was to look into a stronger etchant. HF is a very strong SiO_2 etchant and thus warranted an investigation into its comparable efficacy as a fabrication strategy versus KOH. Two disadvantages to using HF as an etchant are that HF etches so rapidly that the etching process is not as easily revealed and that safety/environmental concerns surrounding use of HF are magnified. HF etching was carried out by pipetting a droplet of HF atop the deposition, leaving it for one minute, then rinsing several times with ethanol. First, to show the validity of this approach, a monolayer of particles is deposited from a purely SiO_2 suspension. Etching this layer (Figure 7a) shows the ability to selectively etch SiO_2. Figure 7b shows a double layer deposited from a binary SiO_2/PS suspension with PS subsequently melted. HF can be used to selectively spatially etch SiO_2 without degrading PS. Here, a portion of the bilayer thin film is etched with fingers of PS extending into the void region where the membrane was fractured. Figure 7c presents a top-down view of an etched SiO_2/PS bilayer with long-range

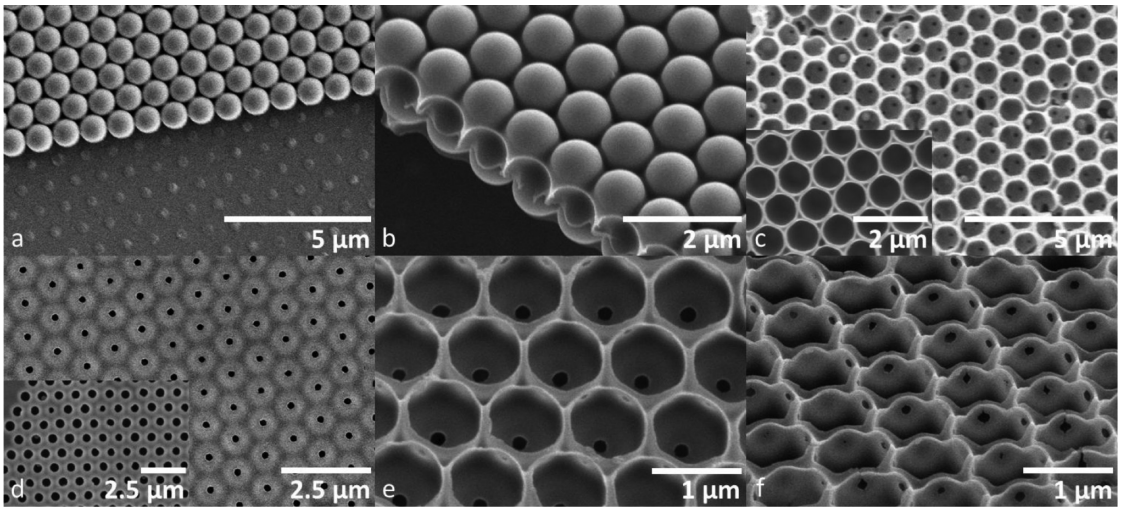

Figure 7. SEM imagery showing the validity of this membrane-fabrication approach. Samples were etched for 1 min while at room temperature. (a) SiO_2 monolayer partially etched using HF. (b) Binary SiO_2/PS bilayer etched and showing fingers of PS bracketing the SiO_2 voids. All other images show monolayer depositions. (c) Top-down views of membranes with some pores visible. (d–f) PS membranes highlighting the interconnecting cavity pores and PS wetting around the SiO_2 microspheres on a tilted SEM stage.

order. The inset shows an etched monolayer. Images d and e in Figure 7 highlight the monodispersity and regularity of the membrane as well as pore locations stemming from SiO_2 contact points. Figure 7d presents etched thin films where microspheres cavities are highly covered with polystyrene. Images e and f in Figure 7 also shows the PS wetting around each of the SiO_2 microspheres and that impact on the resulting membrane morphology—the PS wets higher directly above microsphere contact points than in-between. In addition, one advantage of depositing SiO_2 alongside a polymer onto glass is that the membranes are easy to handle because that glass substrate, SiO_2 itself, etches along with the microspheres causing the membranes to delaminate from that base and float to the top of the KOH bath for simple recovery. Figure 8

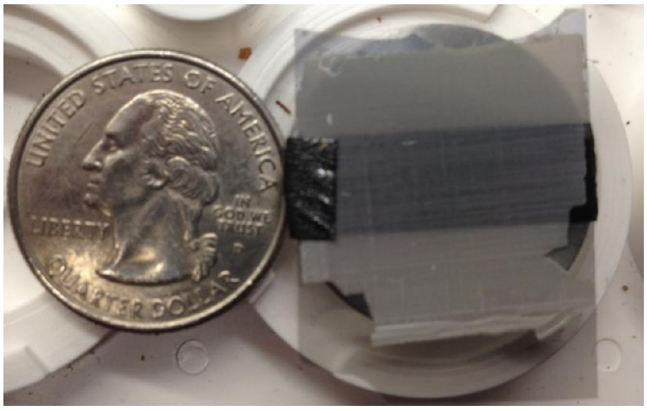

Figure 8. Photo showing a six-layer membrane, synthesized through three depositions at 1/2 v_{mono}, prepared for SEM analysis. Membranes are mechanically strong enough to be easily handled.

presents a photo of a typical 6-layer membrane removed from its etchant bath then placed atop an aluminum support for SEM analysis in order to demonstrate typical membrane size and mechanical robustness. As our convective deposition process is highly scalable, so will be membrane size.

In a given membrane, there are two sizes of pores. Where microspheres contacted one another, you have cavity–cavity pores. Where microspheres contacted the substrate, you have cavity–substrate pores. The pore size ratio is determined by a simple geometric relation of smaller to larger constituents which determines the available angles for smaller particles to pack into the interstices of the larger particles (eqs 2 and 3). Experimentally, 1 μm SiO_2 microspheres coupled with 100 nm PS nanoparticles yield substrate-cavity pores with 200 ± 8 (1 standard deviation) nm diameter, cavity–cavity pores with 141 ± 10 nm diameter and a resulting pore size ratio of 1.42 ± 0.12. Membranes were fabricated with 500 nm SiO_2 and 100 nm PS and exhibited substrate–cavity pores with 149 ± 7 nm diameter, cavity–cavity pores with 104 ± 5 nm, and a resulting pore size ratio of 1.45 ± 0.11. With identical size ratios, k = 0.1, 0.2, eq 3 yields pore size ratios of 1.40 and 1.39, respectively—these ratios correlate very well with the experimental data. For a more in-depth look at this theory, see the Supporting Information.

$$k = \frac{R_2}{R_1} = \text{particle size ratio} \tag{2}$$

$$\text{pore size ratio} = \frac{\tan^{-1}\sqrt{2k + k^2}}{2\tan^{-1}\frac{\sqrt{k}}{2}} \tag{3}$$

These membranes can be easily functionalized for cell, viral, or other bioparticle capture depending on need. Convectively deposited SiO_2 microspheres have already been successfully functionalized with antibodies for cell capture experiments.[57−59] Similarly, PS and other polymers can be labeled with antibodies for targeted biomolecular immobilization.[60,61] Coupling this ability to functionalize membrane constituents with the materials flexibility and tunable pore size gives an enormously versatile membrane fabrication process. Obviously, for filtration experiments factors such as internal concentration polarization and fouling will come into play. One unique advantage of the rapid convective deposition is that this process is scalable by varying the sizes of the blade and substrate and volume of suspension. Additionally, it can easily be modified into a continuous process for industrial applications by

continuously pumping suspension into the corner flow between the blade and substrate.

CONCLUSION

This study investigated the use of binary convective deposition to fabricate macroporous membranes with highly ordered pores of a narrow size distribution. One of the greatest strengths of convective deposition as a method for membrane fabrication is the sheer versatility and tunability of the process. Stepping back from the aforementioned variations that show the huge variety of fabrication techniques and the robustness of the convective deposition technique for the fabrication of multilayer thin films, very small variations in materials can yield enormous flexibility. Binary SiO_2/PS suspensions were convectively deposited with subsequent selectively removal of SiO_2 with KOH and HF. Through depositions with monolayer and multilayer morphologies, membranes of definable thickness with controllable pore and cavity sizes are fabricated. The issue of uniform pore size that so plagues many macroporous membranes of intermediate size is a nonissue with this strategy, and the mechanical stability and physical robustness of these membranes makes them easier to handle than their more fragile counterparts. These membranes are hugely versatile and highly repeatable; they highlight the proven techniques in which these laboratories are already experienced which enhance separations capabilities to target specific cells, viruses, and other receptor-laden bioparticles. Having already machined a suitable testing platform, the next step is to test the efficacy of these membranes with nanoparticle and pseudovirus suspensions.

ASSOCIATED CONTENT

Supporting Information

Supporting Information and derivations are available regarding pore size theory for 1 μm SiO_2/100 nm PS and 500 nm SiO_2/100 nm PS membranes. Additionally, SEM imagery highlighting pore sizes in both conditions is provided. This information is available free of charge via the Internet at http://pubs.acs.org/.

AUTHOR INFORMATION

Corresponding Author

*Telephone: (610) 758-4781. Fax: (610) 758-5057. E-mail: Gilchrist@lehigh.edu.

Notes

The authors declare no competing financial interest.

ACKNOWLEDGMENTS

We gratefully acknowledge the support of the National Science Foundation under award number 0828426. P.K. is grateful for support under the Royal Thai Scholars program. Also we would like to thank Lehigh University and the Howard Hughes Medical Institute for their support of the Biosystems Dynamics Summer Institute at Lehigh University and specifically Sherwood Benavides, Colleen Curley, Jonathan Cursi, and Meaghan Phipps for their work through the summer 2010 BDSI program. We also thank Mark Snyder and Eric Daniels for their comments.

REFERENCES

(1) Burnouf, T.; Radosevich, M. *Haemophilia* **2003**, *9*, 24−37.
(2) Christy, C.; Vermant, S. *Desalination* **2002**, *147*, 1−4.
(3) Desai, T. A.; Hansford, D. J.; Leoni, L.; Essenpreis, M.; Ferrari, M. *Biosens. Bioelectron.* **2000**, *15*, 453−462.
(4) Baker, L. A.; Choi, Y.; Martin, C. R. *Curr. Nanosci.* **2006**, *2*, 243−255.
(5) Zhang, K.; Wu, X. Y. *Biomaterials* **2004**, *25*, 5281−5291.
(6) Park, Y. J.; Ku, Y.; Chung, C. P.; Lee, S. J. *J. Controlled Release* **1998**, *51*, 201−211.
(7) Desai, T. A.; Hansford, D.; Ferrari, M. *J. Membr. Sci.* **1999**, *159*, 221−231.
(8) Risbud, M. V.; Bhonde, R. R. *J. Biomed. Mater. Res.* **2001**, *54*, 436−444.
(9) Clark, W. R.; Hamburger, R. J.; Lysaght, M. J. *Kidney Int.* **1999**, *56*, 2005−2015.
(10) Lopez, C. A.; Fleischman, A. J.; Roy, S.; Desai, T. A. *Biomaterials* **2006**, *27*, 3075−3083.
(11) Norman, J.; Desai, T. *Ann. Biomed. Eng.* **2006**, *34*, 89−101.
(12) Malik, D. J.; Webb, C.; Holdich, R. G.; Ramsden, J. J.; Warwick, G. L.; Roche, I.; Williams, D. J.; Trochimczuk, A. W.; Dale, J. A.; Hoenich, N. A. *Sep. Purif. Technol.* **2009**, *66*, 578−585.
(13) Létant, S. E.; Hart, B. R.; Van Buuren, A. W.; Terminello, L. J. *Nat. Mater.* **2003**, *2*, 391−396.
(14) van de Merbel, N. C. *J. Chromatogr., A* **1999**, *856*, 55−82.
(15) vandeWitte, P.; Dijkstra, P. J.; vandenBerg, J. W. A.; Feijen, J. *J. Membr. Sci.* **1996**, *117*, 1−31.
(16) Adiga, S. P.; Curtiss, L. A.; Elam, J. W.; Pellin, M. J.; Shih, C. C.; Shih, C. M.; Lin, S. J.; Su, Y. Y.; Gittard, S. A.; Zhang, J.; Narayan, R. J. *JOM* **2008**, *60*, 26−32.
(17) Ulbricht, M. *Polymer* **2006**, *47*, 2217−2262.
(18) van den Boogaart, M. A. F.; Kim, G. M.; Pellens, R.; van den Heuvel, J. P.; Brugger, J. *J. Vac. Sci. Technol., B* **2004**, *22*, 3174−3177.
(19) Bwana, N. N.; Leigh, P. *J. Nanopart. Res.* **2008**, *10*, 353−356.
(20) Yang, S. Y.; Ryu, I.; Kim, H. Y.; Kim, J. K.; Jang, S. K.; Russell, T. P. *Adv. Mater.* **2006**, *18*, 709−712.
(21) Thurn-Albrecht, T.; Steiner, R.; DeRouchey, J.; Stafford, C. M.; Huang, E.; Bal, M.; Tuominen, M.; Hawker, C. J.; Russell, T. *Adv. Mater.* **2000**, *12*, 787−791.
(22) Olson, D. A.; Chen, L.; Hillmyer, M. A. *Chem. Mater.* **2008**, *20*, 869−890.
(23) Li, A. P.; Muller, F.; Birner, A.; Nielsch, K.; Gosele, U. *J. Appl. Phys.* **1998**, *84*, 6023−6026.
(24) Li, F. Y.; Zhang, L.; Metzger, R. M. *Chem. Mater.* **1998**, *10*, 2470−2480.
(25) Lee, W.; Schwirn, K.; Steinhart, M.; Pippel, E.; Scholz, R.; Gosele, U. *Nature Nanotechnol.* **2008**, *3*, 234−239.
(26) Yuan, Z. Y.; Su, B. L. *J. Mater. Chem.* **2006**, *16*, 663−677.
(27) Wu, Y. Y.; Cheng, G. S.; Katsov, K.; Sides, S. W.; Wang, J. F.; Tang, J.; Fredrickson, G. H.; Moskovits, M.; Stucky, G. D. *Nat. Mater.* **2004**, *3*, 816−822.
(28) Yamaguchi, A.; Teramae, N. *Anal. Sci.* **2008**, *24*, 25−30.
(29) Wickramasinghe, S. R.; Bower, S. E.; Chen, Z.; Mukherjee, A.; Husson, S. M. *J. Membr. Sci.* **2009**, *340*, 1−8.
(30) Black, C. T.; Guarini, K. W.; Breyta, G.; Colburn, M. C.; Ruiz, R.; Sandstrom, R. L.; Sikorski, E. M.; Zhang, Y. *J. Vac. Sci. Technol., B* **2006**, *24*, 3188−3191.
(31) Tsai, H.; Huang, D.; Ruaan, R.; Lai, J. *Ind. Eng. Chem. Res.* **2001**, *40*, 5917−5922.
(32) Athens, G. L.; Ein-Eli, Y.; Chmelka, B. F. *Adv. Mater.* **2007**, *19*, 2580−2587.
(33) Bouhabila, E. H.; Aim, R. B.; Buisson, H. *Sep. Purif. Technol.* **2001**, *22*−*3*, 123−132.
(34) Unnikrishnan, S.; Jansem, H.; Berenschot, E.; Elwenspoek, M. *Micromechanics Europe* **2007**, *16*, 127−130.
(35) Eyal, A. M.; Hadju, K.; Hazan, B.; Edelstein, D. *J. Appl. Polym. Sci.* **1992**, *46*, 1621−1629.
(36) Wu, S.; Frederic, K. J.; Talarico, M.; Kee, D. D. *Can. J. Chem. Eng.* **2009**, *87*, 579−583.
(37) Baniel, A.; Eyal, A.; Edelstein, D.; Hadju, K.; Hazan, B.; Ilan, Y.; Zamir, E. *J. Membr. Sci.* **1990**, *54*, 271−283.

(38) Jiang, P.; McFarland, M. J. *J. Am. Chem. Soc.* **2005**, *127*, 3710−3711.
(39) van Blaaderen, A.; Hoogenboom, J. P.; Vossen, D. L. J.; Yethiraj, A.; van der Horst, A.; Visscher, K.; Dogterom, M. *Faraday Discuss.* **2003**, *123*, 107−119.
(40) Lee, W.; Chan, A.; Bevan, M. A.; Lewis, J. A.; Braun, P. V. *Langmuir* **2004**, *20*, 5262−5270.
(41) Biancaniello, P. L.; Crocker, J. C. *Rev. Sci. Instrum.* **2006**, *77*, 113702−113702−10.
(42) Hayward, R. C.; Saville, D. A.; Aksay, I. A. *Nature* **2000**, *404*, 56−59.
(43) Dimitrov, A. S.; Nagayama, K. *Chem. Phys. Lett.* **1995**, *243*, 462−468.
(44) Shimmin, R. G.; DiMauro, A. J.; Braun, P. V. *Langmuir* **2006**, *22*, 6507−6513.
(45) Diao, J. J.; Hutchison, J. B.; Luo, G. H.; Reeves, M. E. *J. Chem. Phys.* **2005**, *122*, 184710−1−184710−5.
(46) Boudreau, L. C.; Kuck, J. A.; Tsapatsis, M. *J. Membr. Sci.* **1999**, *152*, 41−59.
(47) Bohaty, A. K.; Abelow, A. E. *J. Porous Mater* **2011**, *18*, 297−304.
(48) Yuan, Y.; Burckel, D. B.; Atanassov, P.; Fan, H. *J. Mater. Chem.* **2006**, *16*, 4637−4641.
(49) Lee, S. B.; Mitchell, D. T.; Trofin, L.; Nevanen, T. K.; Söderlund, H.; Martin, C. R. *Science* **2002**, *296*, 2198−2200.
(50) Kumnorkaew, P.; Ee, Y.; Tansu, N.; Gilchrist, J. F. *Langmuir* **2008**, *24*, 12150−12157.
(51) Velev, O. D.; Lenhoff, A. M. *Curr. Opin. Colloidal Interface Sci.* **2000**, *5*, 56−63.
(52) Kumnorkaew, P.; Weldon, A. L.; Gilchrist, J. F. *Langmuir* **2010**, *26*, 2401−2405.
(53) Kumnorkaew, P.; Gilchrist, J. F. *Langmuir* **2009**, *25*, 6070−6075.
(54) Brewer, D. S.; Allen, J.; Miller, M. R.; Santos, J. M.; Kumar, S.; Norris, D. J.; Tsapatsis, M.; Scriven, L. E. *Langmuir* **2008**, *24*, 13683−13693.
(55) Seidel, H.; Csepregi, L.; Heuberger, A.; Baumgartel, H. *J. Electrochem. Soc.* **1990**, *137*, 3612−3626.
(56) Prevo, B. G.; Velev, O. D. *Langmuir* **2004**, *20*, 2099−2107.
(57) Cheng, X.; Irimia, D.; Dixon, M.; Sekine, K.; Demirci, U.; Zamir, L.; Tompkins, R. G.; Rodriguez, W.; Toner, M. *Lab Chip* **2007**, *7*, 170−178.
(58) Cheng, X.; Liu, Y.; Irimia, D.; Demirci, U.; Yang, L.; Zamir, L.; Rodriguez, W. R.; Toner, M.; Bashir, R. *Lab Chip* **2007**, *7*, 746−755.
(59) Wang, B.; Weldon, A. L.; Kumnorkaew, P. K.; Xu, B.; Gilchrist, J. F.; Cheng, X. *Langmuir* **2011**, *27*, 11229−11237.
(60) Lunov, O.; Syrovets, T.; Loos, C.; Beil, J.; Delacher, M.; Tron, K.; Nienhaus, G. U.; Musyanovych, A.; Mailander, V.; Landfester, K.; Simmet, T. *ACS Nano* **2011**, *5*, 1657−1669.
(61) Peterman, J. H.; Tarcha, P. J.; Chu, V. P.; Butler, J. E. *J. Immunol. Methods* **1988**, *111*, 271−275.